Time-dependent simulation of photocurrent-detected two-dimensional spectroscopy of open systems

Qizhou Chen, Yan Ho Kwok, Weijun Zhou, et al.

ARTICLES YOU MAY BE INTERESTED IN

Time-dependent simulation of photocurrent-detected two-dimensional spectroscopy of open systems

Qizhou Chen,[1,2] (iD) Yan Ho Kwok,[1,3] (iD) Weijun Zhou,[1,3] Guanhua Chen,[1,2,a)] (iD) and Shaul Mukamel[4,a)] (iD)

AFFILIATIONS

[1] Department of Chemistry, The University of Hong Kong, Pok Fu Lam Road, Hong Kong, China
[2] Hong Kong Quantum AI Lab Limited, Hong Kong, China
[3] QuantumFabless Limited, Hong Kong, China
[4] Department of Chemistry, Department of Physics and Astronomy, University of California, Irvine, California 92617, USA

a) Authors to whom correspondence should be addressed: ghc.hku@gmail.com and smukamel@uci.edu

ABSTRACT

A new time-domain simulation protocol of two-dimensional electronic spectra with photocurrent detection is presented. Time-dependent density functional theory for open systems at finite temperature is applied to evaluate the photocurrent response to four laser pulses, and a non-perturbative phase-matching approach is implemented to extract the fourth-order photocurrent signal with a desired phase-matching condition. Simulations for an open three-level model indicates that transition dipoles interact resonantly with the incident pulses and that different sample–electrode couplings may be identified by appearance of different peaks/valleys in photocurrent spectra from different electrodes. Moreover, qualitative reproduction of experimental spectra of a PbS quantum dot photocell [Karki *et al.*, Nat. Commun. **5**(1), 5869 (2014)] reveals the stimulated electron dynamics.

Published under an exclusive license by AIP Publishing. https://doi.org/10.1063/5.0067362

I. INTRODUCTION

Multi-dimensional spectroscopy has been established as a powerful tool for studying materials' electronic and optical properties by nonlinear light–matter interaction,[1] which carries detailed information on energy structures and quantum dynamics for materials.[2–7] The technique involves multiple laser pulses that interact with the sample and measuring the non-linear response. This response as a function of the time intervals between successive laser pulses is then Fourier transformed and displayed as a two-dimensional frequency-domain plot.[1,8] Two-dimensional electronic spectroscopy (2DES) where three pulses are applied to generate the third-order coherent optical response that consists of Ground-State Bleach (GSB), Stimulated Emission (SE), and Excited-State Absorption (ESA)[8] components has been widely used experimentally and theoretically to study charge and energy dynamics of molecular aggregates and materials.[9–15] In 2013, two-dimensional photocurrent spectroscopy (2PCS) that measures currents rather than an optical field has

been used to investigate excitonic resonances in a semiconductor nanostructure.[16] Compared to 2DES, 2PCS applies a fourth pulse to convert the coherent responses into population states to generate fourth-order photocurrent signals. GSB, SE, and ESA also contribute to 2PCS. However, there are two types of ESA responses that contribute oppositely to 2PCS resulting from different interaction paths with the fourth pulse.[4,8] In 2PCS, similar to 2DES, normally the diagonal peaks simply correspond to those seen in photocurrent spectra, whereas the off-diagonal peaks/valleys reveal the coherences among different energy levels. Variation of the photocurrent spectra with the second (population) time interval may reveal the electron dynamics timescale.[4]

2PCS has several merits in the study of ultrafast dynamics in photovoltaic samples. 2DES of bulky samples collects the stimulated optical signals in a given phase-matching direction, but this does not apply to single nanostructures.[16] Instead, 2PCS collects the induced current flow from the sample to electrodes rather than the emitted optical field.[4] Two-dimensional fluorescence spectroscopy

(2DFS) may also detect the stimulated exciton population, but 2PCS may reveal additional light–matter interaction pathways than 2DFS since rapid charge separation before non-radiative Auger recombination may result in much higher quantum yields for photocurrent than for fluorescence.[4] Recently, 2PCS has been applied to measure the ultrafast charge separations by probing the couplings between donors and acceptors during photocurrent generations in organic photocell.[17]

Several techniques have been proposed for simulating nonlinear spectroscopy, which may provide valuable information on the energy landscape and electron dynamics. In the perturbative approach, different types of response signals are evaluated separately through their respective Liouville space pathways, which involves multiple time integrations,[1] and the electric fields are taken to be sequences of temporally well-separated pulses.[1,8] It has been applied to 2DES in order to probe exciton dynamics of multi-chromophoric systems[10] and deactivation pathways of DNA nucleobases.[18] This method enables direct evaluation of each contribution to the nonlinear signal, but for high-order responses such as fourth-order photocurrent signals[4,16] and six-wave-mixing optical signals,[19,20] the required multiple integrations become computationally expensive.[21] In the alternative non-perturbative approach, the time-dependent Schrödinger equation of the driven system is solved and phase-cycling[22] or phase-matching scheme[21] are used to extract the desired response signals.[21] The phase-matching scheme automatically includes effect of pulse shape, duration, and pulse overlaps.[21,23,24] It has been applied to 2DES in the study of population dynamics of the Fenna–Matthews–Olson complex,[25] coupled exciton-vibrational dynamics,[26] and energy transfer dynamics for light harvesting complex.[27,28] It would be useful to apply this method for 2PCS in order to study charge dynamics for open photovoltaic samples, but so far little work has been performed in this direction.

In this paper, we combine our time-dependent density functional theory for open systems (TDDFT-OS) at finite temperature[29–32] with the non-perturbative phase-matching approach[21] to develop a new first-principles methodology for 2PCS simulations. First, the TDDFT-OS formalism for general time-domain simulation of photocurrent responses at finite temperature is introduced. The phase-matching approach is then applied to extract the fourth-order photocurrent response for 2PCS. Finally, the validity of our method is demonstrated by simulation on an open three-level model to demonstrate properties of 2PCS and qualitative reproduction of experimental 2PCS for the PbS quantum dot[4] that shows its electron dynamics for various population times.

II. METHODOLOGY

A. TDDFT-OS protocol for time-domain photocurrent simulations

Consider a typical open electronic system that consists of a sample D coupled to two semi-infinite electrodes L and R. The effective single-electron Hamiltonian and reduced single-electron density matrix (RSDM) of the entire system are partitioned as

$$h(t) = \begin{bmatrix} h_L(t) & h_{LD}(t) & 0 \\ h_{DL}(t) & h_D(t) & h_{DR}(t) \\ 0 & h_{RD}(t) & h_R(t) \end{bmatrix},$$

$$\sigma(t) = \begin{bmatrix} \sigma_L(t) & \sigma_{LD}(t) & 0 \\ \sigma_{DL}(t) & \sigma_D(t) & \sigma_{DR}(t) \\ 0 & \sigma_{RD}(t) & \sigma_R(t) \end{bmatrix}. \tag{1}$$

We assume for simplicity that the two electrodes are not coupled directly to each other. The sample Hamiltonian $h_D(t)$ can be written as

$$h_D(t) = h_D(0) + \delta V(t) + V_{ext}(t). \tag{2}$$

Here, $h_D(0)$ represents the sample Hamiltonian matrix, and $\delta V(t)$ consists of Hartree and exchange–correlation components. $V_{ext}(t)$ represents the time-dependent external potential due to the incident laser pulses. The dipole approximation is invoked, $V_{ext}(t) = \mu \cdot E(t)$, where μ is the transition dipole matrix and $E(t)$ is the electric field due to the incident laser pulses.[8]

The Liouville–von Neumann equation for the RSDM of our open system then reads

$$i\hbar \frac{d}{dt}\sigma_D(t) = [h_D(t), \sigma_D(t)] - \sum_{\alpha=L,R} Q_\alpha(t), \tag{3}$$

$$Q_\alpha(t) \equiv \sigma_{D\alpha}(t)h_{\alpha D}(t) - h_{D\alpha}(t)\sigma_{\alpha D}(t). \tag{4}$$

Here, $Q_\alpha(t)$ is the dissipative term describing the charge and energy transfer between the sample and electrodes. Its trace gives the time-dependent current passing from sample into electrode α,

$$J_\alpha(t) = i\frac{e}{\hbar} \text{Tr}[Q_\alpha(t)]. \tag{5}$$

We shall employ the wide-band-limit approximation[33] for the electrodes. Using the Padé decomposition of Fermi–Dirac distribution function at finite temperature,[34] the dissipative terms $Q_\alpha(t)$ can be expressed as a finite sum of auxiliary matrices,

$$Q_\alpha(t) = \varphi_\alpha(t) - \varphi_\alpha^\dagger(t), \tag{6}$$

$$\varphi_\alpha(t) = \frac{i}{4}[2\sigma_D(t) - I]\Gamma_\alpha + \sum_{p=1}^{N_\alpha} \varphi_{\alpha,p}(t). \tag{7}$$

Here, Γ_α describes the sample coupling to electrode α, I is the identity matrix, and $\varphi_{\alpha,p}(t)$ is the decomposed auxiliary matrix,

$$\varphi_{\alpha,p}(t) = -i\frac{R_{\alpha,p}}{\beta} \int_{-\infty}^{\infty} d\tau\, G_D^r(t,\tau)\Gamma_\alpha e^{-\frac{i}{\hbar}\left(\mu_\alpha + i\frac{z_{\alpha,p}}{\beta}\right)(\tau-t)}. \tag{8}$$

We then obtain the following equation of motion:

$$i\hbar \frac{d}{dt}\varphi_{\alpha,p}(t) = -i\frac{R_{\alpha,p}}{\beta}\Gamma_\alpha + \left[h_D(t) - \frac{i}{2}\sum_\alpha \Gamma_\alpha - \left\{ \mu_\alpha + i\frac{z_{\alpha,p}}{\beta} + \Delta_\alpha(t) \right\} I \right] \varphi_{\alpha,p}(t). \tag{9}$$

Here, $\Delta_\alpha(t)$ denotes the bias voltage of electrode α. Equations (2)–(9) are suitable for time-domain propagation with proper initial conditions. Assuming that initially ($t = 0$) the system is at equilibrium, the initial values of RSDM and auxiliary matrices can be obtained by standard steady-state non-equilibrium Green's function method.

B. Two-dimensional photocurrent spectra and phase matching

Four pulses E_1, E_2, E_3, E_4 are employed to generate the photocurrent signal. Denote the time delays between successive pulses as T_1, T_2, T_3, where T_2 is usually denoted as the population time.[4] The measured time-dependent current through the coupled electrode α, denoted as $J_\alpha(T_1, T_2, T_3, t)$, is parameterized by T_1, T_2, T_3, and the real time t.

Propagating the equations of motion derived in Sec. II A results in the total photocurrent responses.[21] For two-dimensional photocurrent spectra with the typical four-pulse setup, the required response is of the order $O(E_1, E_2, E_3, E_4)$, i.e., the sample will interact once with each of the four pulses. Moreover, signals of different phase-matching conditions capture different dynamical processes and thus reveal different information.[8] We need to extract out of the total current the response with the desired order that satisfies a particular phase-matching condition,

$$k = \pm k_1 \pm k_2 \pm k_3 \pm k_4. \tag{10}$$

For instance, $k = k_1 - k_2 + k_3 - k_4$ is known as the non-rephasing signal, while $k = -k_1 + k_2 + k_3 - k_4$ is known as the rephasing signal.[4,8]

To extract the desired fourth-order response, we run several simulations with each of the pulses switched on or off.[21] Denote $J_{[p_1,p_2,p_3,p_4]}(t)$ as the photocurrent response function resulting from the following incident pulses:

$$E(t) = \sum_{n=1}^{4} p_n E_n(t). \tag{11}$$

Here, $E_n(t)$ denotes the nth pulse function, and p_n is either 0 or 1, indicating that the nth pulse is either on or off, respectively. We need to run the following sixteen simulations to evaluate the fourth-order response, illustrated in Fig. 1. Note that without bias voltage applied on both electrodes, the last term $J_{[0,0,0,0]}(t)$ in Eq. (12) remains zero and therefore can be omitted for evaluation of fourth-order response $J^{(4)}(t)$. However, in general, with bias voltages between electrodes, the steady-state current $J_{[0,0,0,0]}(t)$ may be nonzero,

$$\begin{aligned}
J^{(4)}(t) = &+ J_{[1,1,1,1]}(t) - J_{[1,1,1,0]}(t) - J_{[1,1,0,1]}(t) \\
&- J_{[1,0,1,1]}(t) - J_{[0,1,1,1]}(t) + J_{[1,1,0,0]}(t) + J_{[1,0,1,0]}(t) \\
&+ J_{[1,0,0,1]}(t) + J_{[0,1,1,0]}(t) + J_{[0,1,0,1]}(t) + J_{[0,0,1,1]}(t) \\
&- J_{[1,0,0,0]}(t) - J_{[0,1,0,0]}(t) - J_{[0,0,1,0]}(t) - J_{[0,0,0,1]}(t) \\
&+ J_{[0,0,0,0]}(t).
\end{aligned} \tag{12}$$

The remaining question is how we can extract the photocurrent signal with a specific phase-matching condition,
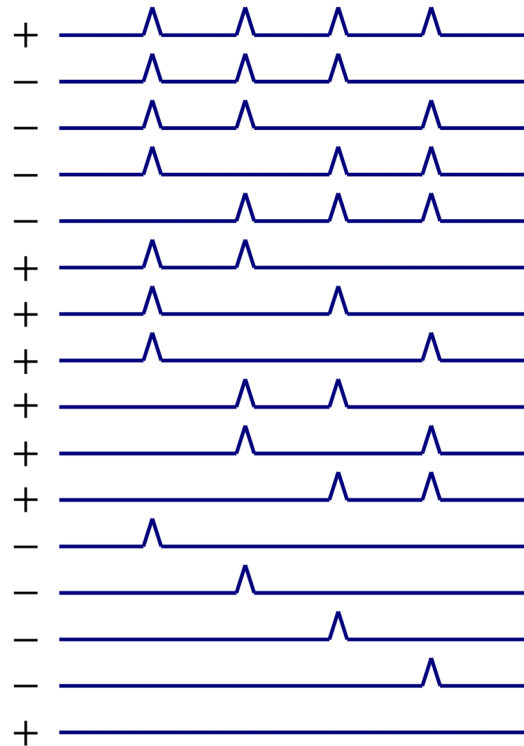

FIG. 1. Schematic diagram to obtain the desired signals of $O(E_1, E_2, E_3, E_4)$ for 2PCS.

such as non-rephasing signal and rephasing signal. Gelin et al. proposed a phase-matching approach,[21] in which the following complex phase-locked[35] electric pulses are applied in the time-dependent Hamiltonian:

$$E_n(r, t) = E_0 B_n(t - t_n) e^{i[k_n \cdot r - m_n \omega_n(t - t_n)]}, \tag{13}$$

$$E(r, t) = \sum_{n=1}^{4} E_n(r, t). \tag{14}$$

Here, $B_n(t)$, k_n, ω_n, and t_n denote the envelope function, wave vector, angular frequency, and envelope center of the nth laser pulse, respectively. The envelope function $B_n(t)$ guarantees that the electric field pulses contain no DC components,[36–38]

$$B_n(t) = e^{-\frac{t^2}{2\sigma^2}} \left(\frac{t}{\omega_n \sigma^2} + i m_n \right). \tag{15}$$

They have shown that by using such a complex electric field, the resulting fourth-order response will satisfy the following phase-matching condition:

$$k = m_1 k_1 + m_2 k_2 + m_3 k_3 + m_4 k_4. \tag{16}$$

The obtained photocurrent signal $J_\alpha^{(4)}(T_1, T_2, T_3, t)$ from Eq. (12) needs to be integrated with respect to the real time t to obtain the rectified current,

$$\bar{J}_\alpha^{(4)}(T_1, T_2, T_3) = \int_0^\infty dt J_\alpha^{(4)}(T_1, T_2, T_3, t). \tag{17}$$

Two-dimensional exponential fitting[39] is then applied to represent $\bar{J}_\alpha(T_1, T_2, T_3)$ along T_1 and T_3, which can save computational cost by proper interpolation and extrapolation (see Appendix A). Fourier transform is then performed with respect to the pulse delay T_1 and T_3 to obtain 2PCS,[4,8]

$$J_\alpha^{(4)}(\omega_{21}, T_2, \omega_{43}) = \int_0^\infty dT_1 e^{ix_1\omega_{21}T_1} \int_0^\infty dT_3 e^{i\omega_{43}T_3} \bar{J}_\alpha^{(4)}(T_1, T_2, T_3). \tag{18}$$

In the Fourier transform with respect to T_1, $x_1 = +1$ is used for the non-rephasing signal and $x_1 = -1$ is used for the rephasing one.[8]

III. SIMULATION RESULTS

A. Calculation for a three-level open model system

To test our protocol, we first simulate a simple three-level model system coupled to two wide-band electrodes, schematically shown in Fig. 2. The lowest level $|0\rangle$ is coupled to the left electrode, the highest level $|2\rangle$ is coupled to the right electrode, and there is a bound state $|1\rangle$ that is not coupled to any electrode. The energies of the three levels are −8065, 8065, and 16 130 cm^{-1}, respectively. The Fermi level in equilibrium is set to be zero. Initially, level $|0\rangle$ is almost fully occupied, while levels $|1\rangle$ and $|2\rangle$ are almost vacant. All optical transitions among these three levels are allowed with identical transition dipole strengths.

Four laser pulses are applied with equal strength E_0 = 0.02 eV/a_0, where a_0 is the Bohr radius. The FWHM of the Gaussian pulse envelope [Eq. (15)] is fixed at 2.5 fs. No bias voltage is applied for both electrodes. To sample the time-domain photocurrent $J_\alpha(T_1, T_2, T_3, t)$, the two pulse intervals T_1 and T_3 are scanned from 0 to 15 fs with 0.3 fs time step, while the interval T_2 is fixed at 5 fs.

Figure 3 shows the 2PCS of the non-rephasing signal $k = k_1 - k_2 + k_3 - k_4$ for both left and right electrodes, obtained by applying laser pulses of different frequencies: 16 130, 20 162, and 24 195 cm^{-1}.

We first compare the 2PCS for the left electrodes. Spectra from 16 130 cm^{-1} pulses have dominant peaks at ω_{21} = 16 130 cm^{-1}. As

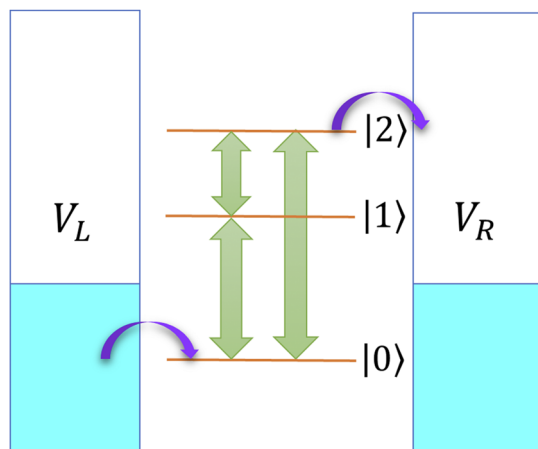the pulse frequency increases, a peak at ω_{21} = 24 195 cm^{-1} gradually appears and becomes dominant for spectra from 24 195 cm^{-1} pulses. Similar analysis for the 2PCS from the right electrodes shows the same effect. Note that initially there are two possible dipole transitions, $|0\rangle \leftrightarrow |1\rangle$ and $|0\rangle \leftrightarrow |2\rangle$, with energy gaps 16 130 and 24 195 cm^{-1}, respectively. As a result, similar to 2DES,[40] different resonant transitions are induced by laser pulses with different frequencies, which accounts for different strengths of peaks/valleys on 2PCS. Similar to 2DES, 2PCS may provide useful information on energy structures and dipole transitions of open quantum samples.

We next compare the 2PCS for the left and right electrodes for the same pulse frequencies. We note that the left and right photocurrent are not symmetric in our model: only $|0\rangle$ is coupled to the left electrode and only $|2\rangle$ is coupled to right one. As a result, for left 2PCS, only peaks/valleys with ω_{43} = 16 130 cm^{-1} and ω_{43} = 24 195 cm^{-1} appear, which corresponds to transitions $|0\rangle \leftrightarrow |1\rangle$ and $|0\rangle \leftrightarrow |2\rangle$, respectively, while the peaks/valleys with ω_{43} = 8065 cm^{-1} for transition $|1\rangle \leftrightarrow |2\rangle$ are missing since none of these two levels are coupled to the left electrode. Similarly, for the right 2PCS, only peaks/valleys with ω_{43} = 8065 cm^{-1} and ω_{43} = 24 195 cm^{-1} appear, which corresponds to transitions $|1\rangle \leftrightarrow |2\rangle$ and $|0\rangle \leftrightarrow |2\rangle$, respectively, while the peaks/valleys with
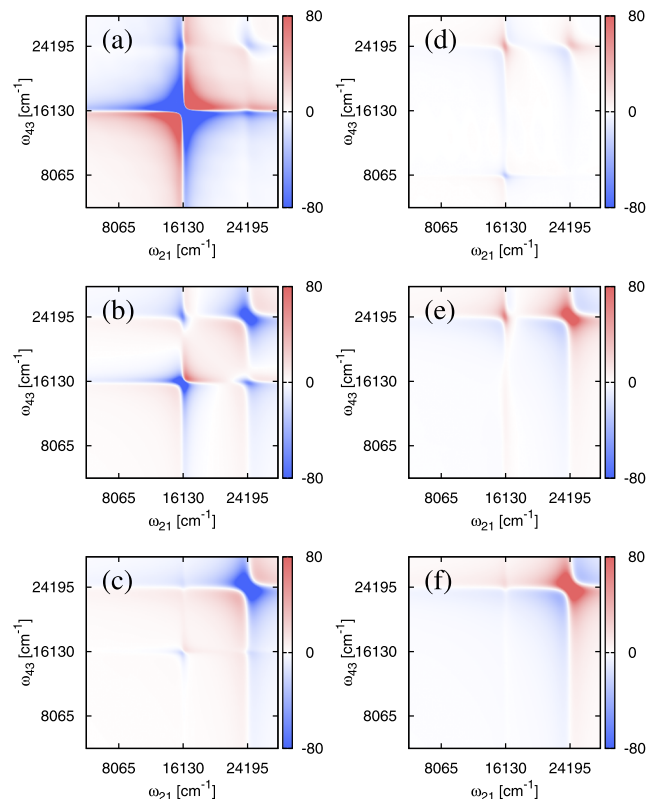

FIG. 3. 2PCS of the three-level model for both electrodes from various pulse frequencies. (a)–(c) result from the left electrodes, while (d)–(f) result from the right ones. Incident pulse frequency reads 16 130, 20 162, and 24 195 cm^{-1} for (a) and (d), (b) and (e), and (c) and (f), respectively.

FIG. 2. Schematic diagram for the three-level model coupled to left and right electrodes.

ω_{43} = 16 130 cm^{-1} for transition $|0\rangle \leftrightarrow |1\rangle$ are missing since these two levels are not coupled to the right electrode. Therefore, 2PCS depends not only on energy structures and dipole transitions of the sample but also on couplings between the sample and the electrodes, and the absence of peaks/valleys for existing dipole transitions in 2PCS for different electrodes may reveal different couplings.

B. Comparison with experimental 2PCS

We next model the experimental 2PCS reported in Ref. 4. Instead of first-principles TDDFT-OS, we employ the open three-level model, which is schematically described in Fig. 4 to reproduce qualitatively the experimental 2PCS.

Karki *et al.* reported 2PCS experiments on the PbS quantum dot coupled to gold electrodes.[4] In one set of experiments, four laser pulses with frequency 14 286 cm^{-1}, which is slightly above the bandgap, are applied and the rephasing signals are collected by phase modulation. Three experiments have been performed to obtain 2PCS for various population time T_2: 0, 0.5, and 1 ps [Figs. 2(a)–2(c) in Ref. 4].

Figure 4 shows the schematic open three-level model. Level $|0\rangle$ represents the ground state in the valence band below the Fermi level, while levels $|1\rangle$ and $|2\rangle$ represent singly excited state and doubly excited state, respectively, in the conduction band continuum above the Fermi level. Consequently, initially level $|0\rangle$ is almost fully occupied, while levels $|1\rangle$ and $|2\rangle$ are almost vacant. The optical transitions $|0\rangle \leftrightarrow |1\rangle$ and $|1\rangle \leftrightarrow |2\rangle$ are allowed with identical transition dipole strength. The energy levels $|1\rangle$ and $|2\rangle$ are picked out so that the energy gaps for both $|0\rangle \leftrightarrow |1\rangle$ and $|1\rangle \leftrightarrow |2\rangle$ are equal to the incident pulse frequency 14 286 cm^{-1} to ensure resonant interactions with the incident pulses. Level $|0\rangle$ is coupled to the left electrode, while levels $|1\rangle$ and $|2\rangle$ are coupled to the right one. Coupling to level $|2\rangle$ is slightly weaker than that to level $|1\rangle$ to ensure the quantum yield for negative ESA contribution is smaller than that for GSB, SE, and positive ESA contributions. However, both couplings for excited states $|1\rangle$, $|2\rangle$ to the right electrode are stronger than the coupling for ground state $|0\rangle$ to the left one, since it should be easier for electrons to migrate in the conduction band.
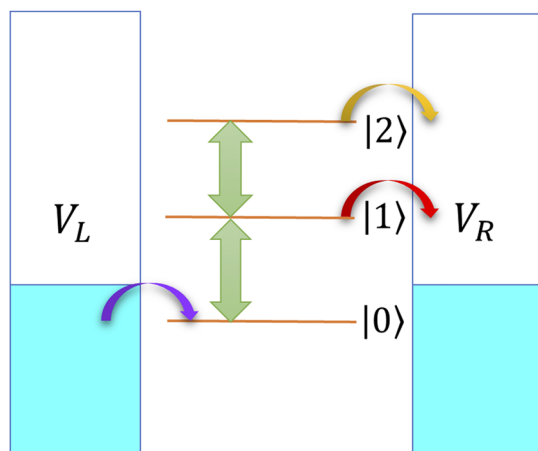
Four laser pulses are applied with equal strength E_0 = 0.04 eV/a_0, where a_0 is the Bohr radius. The FWHM of the Gaussian function for pulse envelope [Eq. (15)] is fixed at 3.5 fs. No bias voltage is applied for both electrodes in these cases. To sample the time-domain photocurrent $J_\alpha(T_1, T_2, T_3, t)$, both pulse intervals T_1 and T_3 are scanned from 0 to 15 fs with a 0.3 fs time step. Rephasing photocurrent signals are collected at the right electrode.

Figure 5 shows the simulated 2PCS for various population time T_2 accordingly. The experimental and simulated 2PCS from our open three-level model are in good agreement for various population time T_2. Since the photon frequency is above the bandgap,[4] valence electrons are expected to interact resonantly with the first two pulses, and consequently, some electrons will jump to the singly excited states in the conduction band, while some will still stay in the original valence states. Karki *et al.* claimed that exciton-induced shift is not significant in this case, so all the energy levels should remain essentially unaltered during the population time T_2.[4] Since the conduction band consists of a broad range of continuous states, their interaction with the last two pulses should also be resonant with the
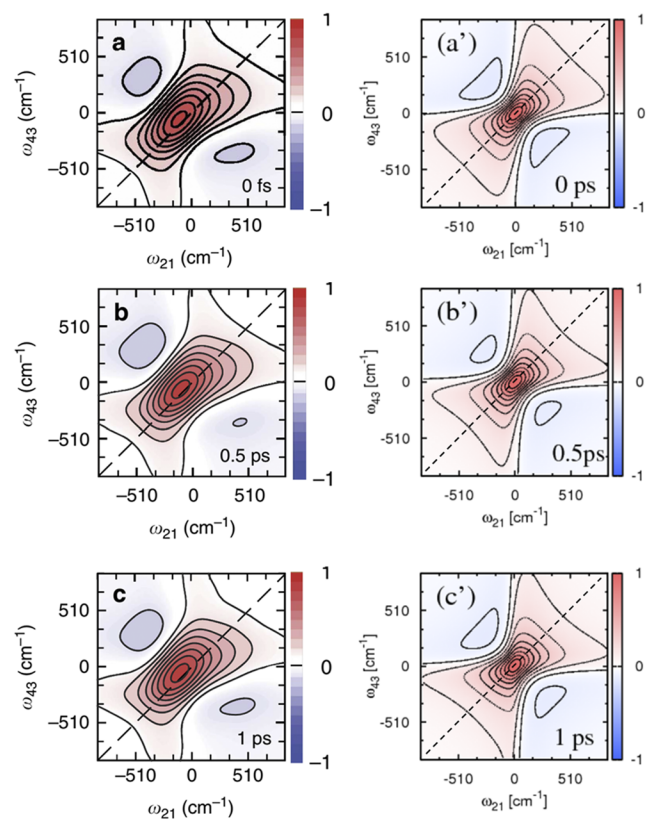
FIG. 5. Comparison of the calculated 2PCS with the experimental results in Ref. 4. (a')–(c') correspond to (a)–(c) [Figs. 2(a)–2(c) in Ref. 4] for $T_2 = 0$, 0.5, 1 ps, respectively. To stay consistent with the experimental 2PCS, for all the reproduction spectra, both axis ω_{21} and ω_{43} are shifted by the pulse frequency 14 286 cm^{-1}. Moreover, all the reproduced 2PCS have been linearly scaled according to their respective ranges. Reprinted with permission from Springer Nature Customer Service Centre GmbH: Springer Nature Nature Communications *Coherent two-dimensional photocurrent spectroscopy in a PbS quantum dot photocell*, Khadga J. Karki *et al.*, 2014. https://www.nature.com/articles/ncomms6869.

FIG. 4. Schematic diagram of the three-level open model for 2PCS reproduction.

pulse frequency 14 286 cm^{-1}. Consequently, some electrons in the singly excited states will jump to doubly excited states, while others may end up in the singly excited states. Finally, exciton populations in both excited states generate photocurrent signals. Therefore, GSB, SE, and ESA responses all contribute peaks/valleys centered at 14 286 cm^{-1} in 2PCS. The quantum yield of the negative ESA contribution should be smaller than those for GSB, SE, and positive ESA contributions, so the resulting signal is a positive peak centered at 14 286 cm^{-1} in 2PCS for various T_2. In our model, electrons in level $|0\rangle$ interact resonantly with the first two pulses, and consequently, some electrons will jump to the singly excited state $|1\rangle$, while some will still stay in level $|0\rangle$. During T_2, all energy levels remain unaltered in this model. The interaction with the last two pulses will then result in electron population in the singly excited state $|1\rangle$ and doubly excited state $|2\rangle$, both of which generate photocurrent signals. All these possible pathways also result in GSB, SE, and ESA contributions to diagonal peak centered at 14 286 cm^{-1} in 2PCS. As is mentioned before, the quantum yield for negative ESA contribution is smaller than those for GSB, SE, and positive ESA contribution, so the diagonal peak in 2PCS remains positive for various T_2.

Note that for experimental 2PCS, the peak position slightly deviates from the diagonal line, which persists for various T_2, while for reproduced 2PCS, such deviation is not observed. Detailed examination of all experimental 2PCS for various T_2 shows that all peaks in 2PCS are actually downshifted for both axis ω_{21} and ω_{43}, but more downshift is observed for ω_{21}, which results in peaks above the diagonal line. In the PbS quantum dot, the valence band may contain a large number of electrons, and therefore, many-body effects should be considered for such deviation. These valence electrons will result in a local repulsion field that partially offsets the positive nuclear attraction. However, this effect is not apparent for states in the conduction band since the population of excited electrons should be much smaller than that for valence electrons. As a result, the oscillation frequency between ground state and singly excited state should decrease slightly, while the frequency between singly excited state and doubly excited state remains essentially unchanged (see Appendix B). Consequently, for GSB and SE contributions, which only involves transitions between ground state and singly excited state,[4] the resulting peaks are downshifted for both axes ω_{21} and ω_{43}, while for both types of ESA contributions, which involves coherences between ground state and singly excited state during T_1 and coherences between singly excited state and doubly excited state during T_3,[4] the resulting peaks/valleys are slightly downshifted for ω_{21} but not for ω_{43}. Therefore, superposition of GSB, SE, and ESA contributions should result in peak downshift for both axes ω_{21} and ω_{43}, but there should be more downshift for ω_{21}, causing the final peaks to position slightly above the diagonal line.

IV. SUMMARY

A first-principles protocol for simulating two-dimensional photocurrent spectra is presented. The TDDFT-OS formalism is implemented to simulate the time-domain photocurrent responses induced by a sequence of laser pulses. A sum of photocurrent responses from certain combinations of pulses can be used to extract the desired fourth-order response, while the application of complex electric field pulses ensures that the fourth-order response satisfies the desired phase-matching condition. Two-dimensional

exponential fitting enables proper interpolation and extrapolation of the rectified photocurrent signal for accurate Fourier transform into two-dimensional photocurrent spectroscopy. Simulation on a simple three-level open model indicates that transition dipoles interact resonantly to incident pulse frequency and that appearance of various peaks/valleys in 2PCS reveals not only the dipole transitions but also the couplings between the sample and electrodes. Moreover, qualitative reproduction for experimental 2PCS for the PbS quantum dot may demonstrate the pulse-induced electron dynamics in such materials for various population times.

AUTHOR DECLARATIONS

Conflict of Interest

The authors have no conflicts to disclose.

DATA AVAILABILITY

The data that support the findings of this study are available from the corresponding authors upon reasonable request.

APPENDIX A: TWO-DIMENSIONAL EXPONENTIAL FITTING FOR 2PCS

To obtain 2PCS, we may simulate the rectified photocurrent signal $\bar{J}_\alpha^{(4)}(T_1, T_2, T_3)$ for a discrete, equal-spacing finite set of T_1 and T_3, while the population time T_2 is a fixed parameter. To save computational cost, we would like to scan only a relatively small range of T_1 and T_3 with grids as coarse as possible. However, the subsequent Fourier transform [Eq. (18)] requires $\bar{J}_\alpha^{(4)}(T_1, T_2, T_3)$ on the whole region where $T_1, T_3 \geq 0$. Moreover, $\bar{J}_\alpha^{(4)}(T_1, T_2, T_3)$ is expected to be essentially a dephasing sinusoidal function with respect to T_1 and T_3. Therefore, it is reasonable to incorporate the two-dimensional exponential fitting technique[39] to approximate $\bar{J}_\alpha^{(4)}(T_1, T_2, T_3)$ for all $T_1, T_3 \geq 0$,

$$\bar{J}_\alpha^{(4)}(T_1, T_2, T_3) \approx \sum_{m=1}^{M} c_m e^{\xi_{m_1} T_1 + \xi_{m_3} T_3}. \tag{A1}$$

Here, ξ_{m_1}, ξ_{m_3} are paired complex exponents with respect to m. The dephasing of $\bar{J}_\alpha^{(4)}(T_1, T_2, T_3)$ with respect to T_1 and T_3 suggests that $\text{Re}[\xi_{m_1}] < 0$ and $\text{Re}[\xi_{m_3}] < 0$.

Suppose we have scanned $(2N_1 + 1) \times (2N_3 + 1)$ equal-spacing sample points with respect to T_1, T_3,

$$T_1 = 0, \Delta T_1, 2\Delta T_1, \ldots, 2N_1 \Delta T_1, \tag{A2}$$

$$T_3 = 0, \Delta T_3, 2\Delta T_3, \ldots, 2N_3\Delta T_3. \tag{A3}$$

Define that

$$z_{m_1} \equiv e^{\frac{\xi_{m_1}}{2N_1}}, \tag{A4}$$

$$z_{m_3} \equiv e^{\frac{\xi_{m_3}}{2N_3}}. \tag{A5}$$

The corresponding Hankel operator h is defined as follows:

$$(hu)(i_1, i_3) = \sum_{\substack{0 \le j_1 \le N_1 \\ 0 \le j_3 \le N_3}} \bar{J}_\alpha^{(4)}[(i_1 + j_1)\Delta T_1, T_2, (i_3 + j_3)\Delta T_3]$$
$$\times u(j_1, j_3) \, i_1 \le N_1, i_3 \le N_3. \tag{A6}$$

The Hankel operator h should have multiple singular vectors, denoted by $\{u_l\}$. Then, the corresponding lth, $(l-1)$th eigenpolynomials read

$$P_l(z_{m_1}, z_{m_3}) = \sum_{\substack{0 \le j_1 \le N_1 \\ 0 \le j_3 \le N_3}} u_l(j_1, j_3) z_{m_1}^{j_1} z_{m_3}^{j_3}, \tag{A7}$$

$$P_{l-1}(z_{m_1}, z_{m_3}) = \sum_{\substack{0 \le j_1 \le N_1 \\ 0 \le j_3 \le N_3}} u_{l-1}(j_1, j_3) z_{m_1}^{j_1} z_{m_3}^{j_3}. \tag{A8}$$

These two polynomials may be solved together by the resultant method for their common roots (z_{m_1}, z_{m_3}).[41] Then, we may use Eqs. (A4) and (A5) to construct the exponents ξ_{m_1}, ξ_{m_3} in Eq. (A1).

Finally, the coefficients c_m may be determined by optimization of the approximation [Eq. (A1)] for all sample points accordingly.[42]

The Fourier transform of a two-dimensional exponential sum is straightforward [Eqs. (18) and (A1)],

$$J_\alpha^{(4)}(\omega_{21}, T_2, \omega_{43}) = \int_0^\infty dT_1 e^{ix_1\omega_{21}T_1}$$
$$\times \int_0^\infty dT_3 e^{i\omega_{43}T_3} \bar{J}_\alpha^{(4)}(T_1, T_2, T_3)$$
$$\approx \sum_{m=1}^M c_m \frac{1}{ix_1\omega_{21} + \xi_{m_1}} \frac{1}{i\omega_{43} + \xi_{m_3}}. \tag{A9}$$

Unfortunately, the computational cost for construction of coefficients c_m and exponents ξ_{m_1}, ξ_{m_3} for two-dimensional exponential fitting would increase dramatically as N_1 and N_3 increase. However, in our case, sufficiently large N_1 and N_3 are necessary to well depict $\bar{J}_\alpha^{(4)}(T_1, T_2, T_3)$. Thus, it becomes impractical to simply fit all the scanned data points [Eqs. (A2) and (A3)] by a single set of two-dimensional exponential functions. The following tokens are implemented to address this problem.

As is shown in Fig. 6, the scanned data region (cyan area) for $\bar{J}_\alpha^{(4)}(T_1, T_2, T_3)$ are partitioned into a number of blocks, where each block is sufficiently small for efficient two-dimensional exponential fitting. For each block, the fitted exponential functions would be used to interpolate the block itself. Additionally, for the block on
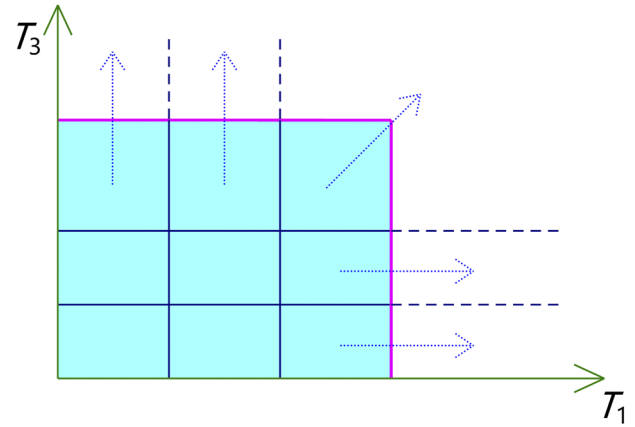

FIG. 6. Partition scheme for two-dimensional exponential fitting.

the edge with pink side(s), the fitted exponential functions would be further used to extrapolate part of the region outside the scanned data region indicated by the respective arrow. In this way, the rectified photocurrent response $\bar{J}_\alpha^{(4)}(T_1, T_2, T_3)$ can be properly approximated by two-dimensional exponential functions for all $T_1, T_3 \ge 0$, which is ready for efficient Fourier transform into 2PCS.

APPENDIX B: MODIFIED OPTICAL BLOCH EQUATIONS FOR PbS QUANTUM DOT

Consider a single valence electron in the PbS quantum dot. Classical electrodynamics gives the potential energy induced by local field from other valence electrons, described by charge density ρ,[43]

$$V(\rho, \mathbf{r}, t) = -\frac{1}{4\pi\epsilon_0} \int \frac{\rho\left(\mathbf{r}', t - \frac{|\mathbf{r}-\mathbf{r}'|}{c}\right)}{|\mathbf{r}-\mathbf{r}'|} d\mathbf{r}'. \tag{B1}$$

Here, the integration is performed over the whole $\mathbf{r}'$ space. Therefore, the Hamiltonian of a single valence electron may be approximated as

$$\mathbf{H}_D' = \begin{bmatrix} \varepsilon_0 & & \\ & \varepsilon_1 & \\ & & \varepsilon_2 \end{bmatrix} + \begin{bmatrix} eV(\rho) & & \\ & 0 & \\ & & 0 \end{bmatrix}. \tag{B2}$$

Here, ε_0, ε_1, and ε_2 are the energy for $|0\rangle$, $|1\rangle$, and $|2\rangle$, respectively. The induced many-body effects for valence bands are approximated by $eV(\rho)$. For the conduction band, this effect should be comparably negligible since population of conduction electrons is expected to be much smaller than that of valence electrons. With electric field pulses $E(t)$ applied on transition dipoles, (B2) is substituted into the Liouville–von Neumann equation[8] to obtain the modified optical Bloch equations for the single-electron density matrix,[44]

$$i\frac{d\sigma_{01}}{dt} = -[(\varepsilon_1 - \varepsilon_0) - eV(\rho)]\sigma_{01}$$
$$+ E(t)[\sigma_{02}\mu_{12} + (\sigma_{00} - \sigma_{11})\mu_{01}], \tag{B3}$$

$$i\frac{d\sigma_{12}}{dt} = -(\varepsilon_2 - \varepsilon_1)\sigma_{12} + E(t)\left[-\sigma_{02}\mu_{01} + (\sigma_{11} - \sigma_{22})\mu_{12}\right]. \quad \text{(B4)}$$

Here, μ_{01} and μ_{12} are transition dipole strength for $|0\rangle \leftrightarrow |1\rangle$ and $|1\rangle \leftrightarrow |2\rangle$, respectively. Therefore, after the interaction with the electric field pulses, σ_{01} would oscillate with frequency $|(\varepsilon_1 - \varepsilon_0) - eV(\rho)|$, which is slightly downshifted by the induced local potential, whereas σ_{12} would still oscillate with frequency $|\varepsilon_2 - \varepsilon_1|$, as is the case without the induced local potential in valence bands.

REFERENCES

[1] S. Mukamel, *Principles of Nonlinear Optical Spectroscopy* (Oxford University Press, New York, 1995).

[2] A. De Sio *et al.*, "Ultrafast relaxation dynamics in a polymer: Fullerene blend for organic photovoltaics probed by two-dimensional electronic spectroscopy," Eur. Phys. J. B **91**(10), 236 (2018).

[3] S. Mueller *et al.*, "Observing multiexciton correlations in colloidal semiconductor quantum dots via multiple-quantum two-dimensional fluorescence spectroscopy," ACS Nano **15**(3), 4647–4657 (2021).

[4] K. J. Karki *et al.*, "Coherent two-dimensional photocurrent spectroscopy in a PbS quantum dot photocell," Nat. Commun. **5**(1), 5869 (2014).

[5] C. Kreisbeck and T. Kramer, "Long-lived electronic coherence in dissipative exciton dynamics of light-harvesting complexes," J. Phys. Chem. Lett. **3**(19), 2828–2833 (2012).

[6] J. Lim *et al.*, "Vibronic origin of long-lived coherence in an artificial molecular light harvester," Nat. Commun. **6**(1), 7755 (2015).

[7] G. A. Lott *et al.*, "Conformation of self-assembled porphyrin dimers in liposome vesicles by phase-modulation 2D fluorescence spectroscopy," Proc. Natl. Acad. Sci. U. S. A. **108**(40), 16521 (2011).

[8] P. Hamm and M. Zanni, *Concepts and Methods of 2D Infrared Spectroscopy* (Cambridge University Press, 2011).

[9] W. Zhao *et al.*, "Optical gain from biexcitons in CsPbBr$_3$ nanocrystals revealed by two-dimensional electronic spectroscopy," J. Phys. Chem. Lett. **10**(6), 1251–1258 (2019).

[10] M. Cho *et al.*, "Exciton analysis in 2D electronic spectroscopy," J. Phys. Chem. B **109**(21), 10542–10556 (2005).

[11] D. Zigmantas *et al.*, "Two-dimensional electronic spectroscopy of the B800–B820 light-harvesting complex," Proc. Natl. Acad. Sci. U. S. A. **103**(34), 12672 (2006).

[12] O. Bixner *et al.*, "Ultrafast photo-induced charge transfer unveiled by two-dimensional electronic spectroscopy," J. Chem. Phys. **136**(20), 204503 (2012).

[13] E. L. Read *et al.*, "Visualization of excitonic structure in the Fenna-Matthews-Olson photosynthetic complex by polarization-dependent two-dimensional electronic spectroscopy," Biophys. J. **95**(2), 847–856 (2008).

[14] R. Tempelaar and T. C. Berkelbach, "Many-body simulation of two-dimensional electronic spectroscopy of excitons and trions in monolayer transition metal dichalcogenides," Nat. Commun. **10**(1), 3419 (2019).

[15] A. Nenov *et al.*, "Two-dimensional electronic spectroscopy of benzene, phenol, and their dimer: An efficient first-principles simulation protocol," J. Chem. Theory Comput. **11**(8), 3755–3771 (2015).

[16] N. Gaël *et al.*, "Multidimensional coherent photocurrent spectroscopy of a semiconductor nanostructure," Opt. Express **21**(23), 28617–28627 (2013).

[17] E. Vella *et al.*, "Two-dimensional coherent photocurrent excitation spectroscopy in a polymer solar cell," arXiv:1506.07837v2, 1–12 (2015).

[18] A. Nenov *et al.*, "Probing deactivation pathways of DNA nucleobases by two-dimensional electronic spectroscopy: First principles simulations," Faraday Discuss. **177**(0), 345–362 (2015).

[19] Y. Zhang, A. W. Brown, and M. Xiao, "Opening four-wave mixing and six-wave mixing channels via dual electromagnetically induced transparency windows," Phys. Rev. Lett. **99**(12), 123603 (2007).

[20] Y. Zhang *et al.*, "Temporal and spatial interference between four-wave mixing and six-wave mixing channels," Phys. Rev. Lett. **102**(1), 013601 (2009).

[21] M. F. Gelin, D. Egorova, and W. Domcke, "Efficient calculation of the polarization induced by *N* coherent laser pulses," J. Chem. Phys. **131**(19), 194103 (2009).

[22] H.-S. Tan, "Theory and phase-cycling scheme selection principles of collinear phase coherent multi-dimensional optical spectroscopy," J. Chem. Phys. **129**(12), 124501 (2008).

[23] Y. Ke and Y. Zhao, "Calculations of coherent two-dimensional electronic spectra using forward and backward stochastic wavefunctions," J. Chem. Phys. **149**(1), 014104 (2018).

[24] X. Leng *et al.*, "Effects of finite laser pulse width on two-dimensional electronic spectroscopy," Chem. Phys. Lett. **667**, 79–86 (2017).

[25] L. Z. Sharp, D. Egorova, and W. Domcke, "Efficient and accurate simulations of two-dimensional electronic photon-echo signals: Illustration for a simple model of the Fenna–Matthews–Olson complex," J. Chem. Phys. **132**(1), 014501 (2010).

[26] L. Z. Sharp and D. Egorova, "Towards microscopic assignment of oscillative signatures in two-dimensional electronic photon-echo signals of vibronic oligomers: A vibronic dimer model," J. Chem. Phys. **139**(14), 144304 (2013).

[27] X. Leng *et al.*, "Simulation of the two-dimensional electronic spectroscopy and energy transfer dynamics of light-harvesting complex II at ambient temperature," J. Phys. Chem. B **122**(17), 4642–4652 (2018).

[28] X. Leng *et al.*, "Hierarchical equations of motion simulation of temperature-dependent two-dimensional electronic spectroscopy of the chlorophyll a manifold in LHCII," Chem. -Asian J. **15**(13), 1996–2004 (2020).

[29] X. Zheng *et al.*, "Time-dependent density-functional theory for open systems," Phys. Rev. B **75**(19), 195127 (2007).

[30] X. Zheng *et al.*, "Time-dependent density functional theory for quantum transport," J. Chem. Phys. **133**(11), 114101 (2010).

[31] S. K. Koo *et al.*, "First-principles Liouville–von Neumann equation for open systems and its applications," Phys. Status Solidi B **249**(2), 270–275 (2012).

[32] Y. Zhang, S. Chen, and G. Chen, "First-principles time-dependent quantum transport theory," Phys. Rev. B **87**(8), 085110 (2013).

[33] A.-P. Jauho, N. S. Wingreen, and Y. Meir, "Time-dependent transport in interacting and noninteracting resonant-tunneling systems," Phys. Rev. B **50**(8), 5528–5544 (1994).

[34] J. Hu *et al.*, "Padé spectrum decompositions of quantum distribution functions and optimal hierarchical equations of motion construction for quantum open systems," J. Chem. Phys. **134**(24), 244106 (2011).

[35] M. F. Gelin and W. Domcke, "Alternative view of two-dimensional spectroscopy," J. Chem. Phys. **144**(19), 194104 (2016).

[36] J. Rauch and G. Mourou, "The time integrated far field for Maxwell's and D'Alembert's equations," Proc. Am. Math. Soc. **134**(3), 851–858 (2006).

[37] T. Brabec and F. Krausz, "Intense few-cycle laser fields: Frontiers of nonlinear optics," Rev. Mod. Phys. **72**(2), 545–591 (2000).

[38] L. Chen *et al.*, "Stark control of electrons along nanojunctions," Nat. Commun. **9**(1), 2070 (2018).

[39] F. Andersson, M. Carlsson, and M. V. de Hoop, "Nonlinear approximation of functions in two dimensions by sums of exponential functions," Appl. Comput. Harmonic Anal. **29**(2), 156–181 (2010).

[40] Y. H. Kwok, "Time-dependent quantum transport: First principles simulations and applications," in *Chemistry* (The University of Hong Kong, 2016).

[41] G. Jónsson and S. Vavasis, "Accurate solution of polynomial equations using Macaulay resultant matrices," Math. Comput. **74**(249), 221–262 (2005).

[42] G. Beylkin and L. Monzón, "On approximation of functions by exponential sums," Appl. Comput. Harmonic Anal. **19**(1), 17–48 (2005).

[43] D. J. Griffiths, *Introduction to Electrodynamics* (Pearson Education, Inc., 2013).

[44] J. M. Shacklette and S. T. Cundiff, "Role of excitation-induced shift in the coherent optical response of semiconductors," Phys. Rev. B **66**(4), 045309 (2002).